ACS Energy LETTERS

Cite This: ACS Energy Lett. 2019, 4, 1394−1400

http://pubs.acs.org/journal/aelccp

LETTER

Degradation Mechanism of Ni-Enriched NCA Cathode for Lithium Batteries: Are Microcracks Really Critical?

Kang-Joon Park,[†] Jang-Yeon Hwang,[†] Hoon-Hee Ryu,[†] Filippo Maglia,[‡] Sung-Jin Kim,[‡] Peter Lamp,[‡] Chong S. Yoon,*[,§] and Yang-Kook Sun*[,†]

[†]Department of Energy Engineering, Hanyang University, Seoul 04763, South Korea

[‡]BMW Group, Petuelring 130, 80788 Munich, Germany

[§]Department of Materials Science and Engineering, Hanyang University, Seoul 04763, South Korea

Supporting Information

ABSTRACT: A series of Ni-enriched $Li[Ni_xCo_yAl_z]O_2$ cathodes (x = 0.80−0.95) were synthesized and evaluated comprehensively to investigate the capacity fading mechanism. Capacity retention was shown to be strongly related to the extent of microcracking within the secondary particles. Moreover, the range and limit of the depth of discharge (DOD), which determined the extent of microcracking, critically affected the cycling stability such that the extremely Ni-rich $Li[Ni_{0.95}Co_{0.04}Al_{0.01}]O_2$ cathode cycled at an upper DOD of 60% exhibited the poorest capacity retention. The anisotropic strain produced by the H2−H3 phase transition was not fully relieved, and persistent microcracks in the discharged state (3.76 V) allowed the electrolyte to penetrate the particle interior. Resultant extended exposure of the interior primary particles within secondary particle to electrolyte attack accelerated structural damage and eventually undermined the mechanical integrity of the cathode particles.

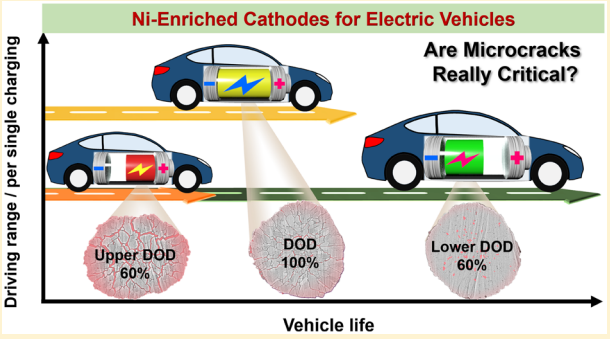

A new trend that has recently gained tremendous momentum in the automobile industry is the development of electric vehicles (EVs). Owing to fluctuating fossil fuel prices and environmental concerns, EVs have been the center of research for many automobile companies, mainly in Europe, Japan, China, and US. Among all the existing batteries of EVs, lithium-ion batteries (LIBs) have become the primary power sources because they have the highest energy density and a long cycle life. Nevertheless, many obstacles still lie ahead for wide consumer acceptance of LIB-based EVs. One of the primary concerns is the limited driving range of EVs. The U.S. Department of Energy has estimated a 300-mile driving range for a single charge as the threshold for the commercial success of EVs.[1] To satisfy the energy density requirement, layered Ni-rich $LiMO_2$ (M = Ni, Co, and Mn (NCM) or Ni, Co, and Al (NCA)) cathodes have been developed extensively for the last two decades because of their high theoretical capacity of 275 mAh g^{-1}.[2−15] Currently, $Li[Ni_{0.8}Co_{0.15}Al_{0.05}]O_2$ and $Li[Ni_{0.6}Co_{0.2}Mn_{0.2}]O_2$ cathodes are adapted for EVs (Tesla Model 3 and GM Bolt) that have a driving range of 380 km for a single charge, which is still short of the recommended threshold. To further increase the driving range, the Ni content in the cathodes should be increased gradually so that the energy density of the LIBs is increased. However, it is well acknowledged that the increase in the Ni concentration of $LiMO_2$ leads to an almost linear increase in the reversible capacity but a proportional decrease in the cycling performance and thermal safety.[11,13,16] The fast capacity fading of Ni-enriched NCMs is ascribed to the H2−H3 phase transition in the highly charged state of approximately 4.2 V Li^+/Li, inducing an anisotropic lattice volume change that generates internal microcracks in the cathode particles.[16−20] The microcracks facilitate electrolyte infiltration into the particle interior. The penetrated electrolyte accelerates surface degradation of the primary particles through the reaction of unstable Ni^{4+} with electrolyte to form NiO-like rocksalt impurity phases and thereby increases the cell impedance.[16,17] The currently deployed cylindrical full cell based on the NCA cathode and graphite anode demonstrates poor long-term cycling performance (capacity retention of 50% after 2000 cycles) when cycled at 100% depth of discharge (DOD). However, the full cell demonstrates an outstanding Li intercalation stability at DOD of 60% during the same cycling

Received: April 5, 2019
Accepted: May 22, 2019
Published: May 23, 2019

DOI: 10.1021/acsenergylett.9b00733
ACS Energy Lett. 2019, 4, 1394−1400

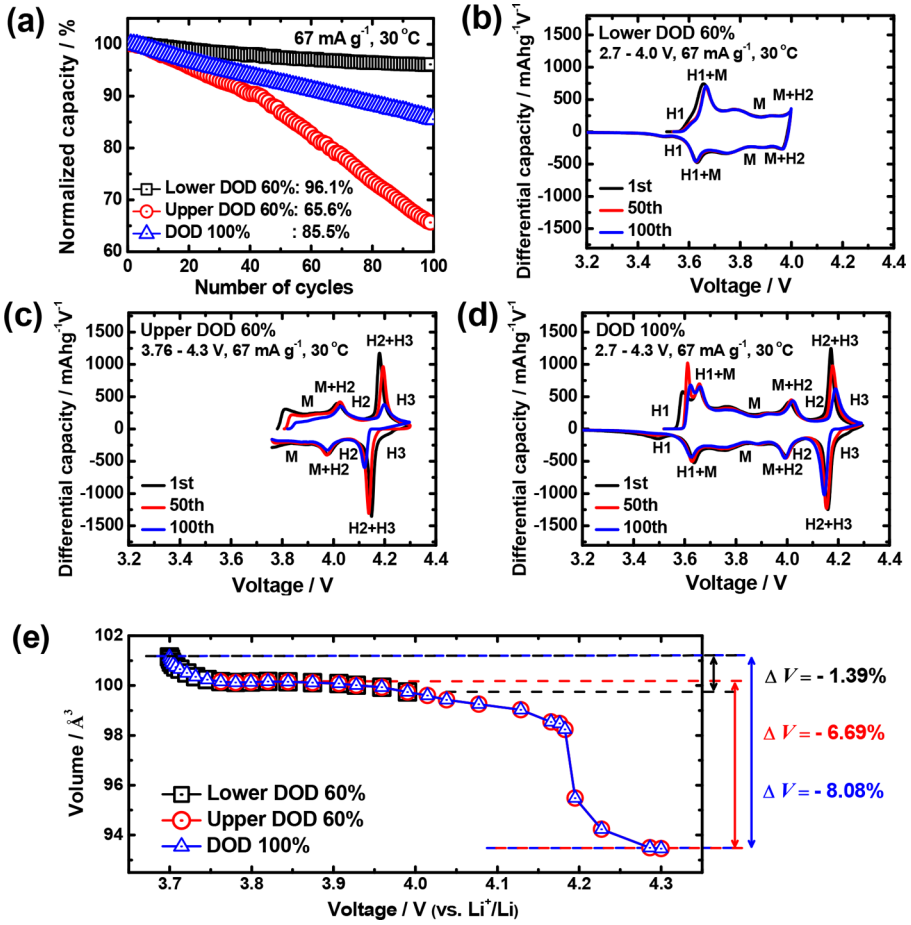

Figure 1. (a) Cycle performances of NCA95 cathodes charged and discharged at different DOD ranges. dQ dV^{-1} curves of NCA95 cathodes cycled at (b) lower DOD of 60%, (c) upper DOD of 60%, and (d) DOD of 100% as a function of number of cycles. (e) Unit cell volume changes for NCA95 cathodes during charging at different DOD ranges. The unit cell volume was calculated from in situ XRD pattern in Figure S4.

period, indicating that the DOD should be limited to 60% for long-term cycling.[21,22] However, limiting the DOD during cycling reduces the energy density of the battery significantly and, consequently, increases the EV's weight and battery cost.

Currently, Tesla, which is one of the most prominent EV producers, uses the Panasonic $Li[Ni_{0.84}Co_{0.12}Al_{0.04}]O_2$ cathode in its Model S and Model X.[23] However, with the increasing demand for higher energy density and the ever-increasing cost of raw cobalt, which has more than doubled in the last five years, increasing the Ni content in the cathode active material has become mandatory. In this regard, we performed a systematic comparative study of the standard $Li[Ni_{0.8}Co_{0.16}Al_{0.04}]O_2$ (herein after denoted as NCA80), $Li[Ni_{0.88}Co_{0.10}Al_{0.02}]O_2$ (NCA88), and $Li[Ni_{0.95}Co_{0.04}Al_{0.01}]O_2$ (NCA95). On the basis of this result, we explore the fundamental battery performance and capacity fade mechanisms of the three NCA cathodes to understand the impact of the increased Ni content on the electrochemical performance of the highly Ni-enriched NCA cathodes.

The chemical compositions of NCA80, NCA88, and NCA95 measured by inductively coupled plasma were $Li[Ni_{0.8}Co_{0.16}Al_{0.04}]O_2$, $Li[Ni_{0.88}Co_{0.10}Al_{0.02}]O_2$, and $Li[Ni_{0.95}Co_{0.04}Al_{0.01}]O_2$, respectively. The XRD patterns in Figure S1 and Rietveld refinement in Table S1 confirm that NCA80, NCA88, and NCA95 have a rhombohedral α-$NaFeO_2$-layered structure with the $R\bar{3}m$ space group and lattice parameters of a = 2.8630 Å and c = 14.1756 Å, a = 2.8679 Å and c = 14.1812 Å, and a = 2.8721 Å and c = 14.1908 Å, respectively. The reversible capacity of NCA80, NCA88, and NCA95 was characterized by 2032 coin-type half-cells using Li metal as the anode cycled between 2.7 and 4.3 V. As shown in Figure S2, the discharge capacity of the three NCA cathodes increased progressively with increasing Ni content owing to the increased amount of redox active Ni ions: 202.5 mAh g^{-1} for NCA80, 219.8 mAh g^{-1} for NCA88, and 236.8 mAh g^{-1} for NCA95.

To investigate the capacity fading mechanism of Ni-rich NCA cathodes, the NCA95 cathode was cycled at the upper (3.76−4.3 V) and lower DOD of 60% (2.7−4.0 V) and DOD of 100% (2.7−4.3 V) with a current density of 67 mA g^{-1} (Figure S3). As shown in Figure 1a, the cycling stability of the NCA95 cathode deteriorated significantly at the upper DOD of 60%, with only 65.6% retention of the initial capacity after 100 cycles as compared to that (85.5%) at the DOD of 100% (2.7−4.3 V). Meanwhile, the NCA cathode cycled at a lower DOD of 60% incurred nearly no capacity fading (96.1%). To verify the different capacity retentions depending on the DOD range, dQ dV^{-1} profiles with cycling were calculated by differentiating the charge/discharge curves (Figure 1b−d). The redox peaks for the H2−H3 phase transition upon cycling at the upper DOD of 60% decayed more rapidly in height than those at a DOD of 100%. Meanwhile, the redox peaks for the H1−M phase transition at the lower DOD of 60% hardly changed with cycling, thus attesting to the stability of the host structure in the lower DOD range. As shown in Figure 1e, the NCA95 cathode suffers from

DOI: 10.1021/acsenergylett.9b00733
ACS Energy Lett. 2019, 4, 1394−1400

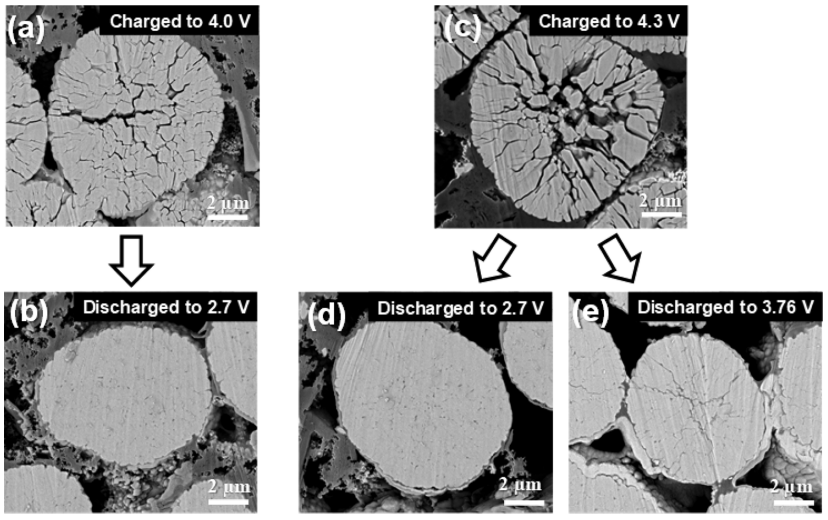

Figure 2. Cross-sectional SEM images of NCA95 cathodes at first cycle: (a) charged to 4.0 V, (b) charged to 4.0 V and discharged to 2.7 V, (c) charged to 4.3 V, (d) charged to 4.3 V and discharged to 2.7 V, and (e) charged to 4.3 V and discharged to 3.76 V.

volume contractions of 1.39%, 6.69%, and 8.08% during charging to 4.3 V for the lower DOD of 60%, upper DOD of 60%, and DOD of 100%, respectively. The unit cell volume of the NCA95 cathode was calculated from in situ XRD patterns in Figure S4. Conventional wisdom dictates that the cycling stability should deteriorate at a higher rate as the anisotropic volume contraction increases in magnitude, which was true in the case of the NCM cathodes;[11,16,17] nevertheless, the NCA95 cathode cycled at the upper DOD of 60% exhibited poorer capacity retention compared to the same cathode cycled at a full DOD range although the former was subject to a smaller magnitude of volume contraction/expansion during cycling compared to the latter. To better understand the discrepancy, cross sections of the NCA95 cathodes charged and discharged at different ranges of DOD (lower and upper DOD of 60%, DOD of 100%) were examined using SEM (Figure 2 and Figure S5). The NCA95 particles charged to 4.0 V contained a large number of microcracks that nearly traversed the entire particle but terminated before reaching the particle surface (Figure 2a). In comparison, the NCA95 cathode particles that were fully charged to 4.3 V contained numerous microcracks propagated through the entire particle to the surface, facilitating electrolyte penetration into the particle interior. These microcracks partially fractured the secondary particle into several smaller segments (Figure 2c). However, surprisingly, when the NCA95 cathode was fully discharged to 2.7 V, the microcracks generated from charging to either 4.0 V (lower DOD of 60%) or 4.3 V (DOD of 100%) closed back and hardly any microcracks were observed in the discharged state (Figure 2b,d). The reason for the crack closure is likely due to the expansion of the primary grains upon lithiation which fills the cracks. The extent of microcracking was estimated using image analysis software by measuring the areas covered by the microcracks. In fact, the areal fraction of the microcracks estimated from the cross-sectional images increased from 11% for the lower DOD of 60% to 26% for the full DOD of 100% and decreased to 1% in the fully discharged state. Figure 2 demonstrates the extent of the mechanical damage sustained by the NCA95 cathode in the charged state, the fact that the catastrophic mechanical failure can be repaired, and that the original microstructure is recovered during the subsequent discharge. A clue for the apparent inferior cycling stability of the NCA95 cycled at the upper DOD of 60% is provided in Figure 2e, which shows a cross-sectional SEM image of the NCA95 discharged to 3.76 V. In contrast to the cathode particles discharged to 2.7 V, clearly visible residual microcracks were observed (microcrack areal fraction 4%). In addition, the microcracks propagated to the particle surface, thus opening up channels for electrolyte infiltration. In our opinion, the electrolyte continues to infiltrate readily along the residual microcracks into the particle core even in the discharged state (3.76 V) and accelerates microcrack formation and the eventual pulverization of the particles.

To substantiate the observation, cross-sectional SEM images of the NCA95 cathode cycled at different DOD ranges are shown in Figure 3 (after 100 cycles and at their respective discharged states). After 100 cycles, the NCA95 cathode cycled particles at a lower DOD of 60% preserved the original spherical morphology without visible microcracks (areal fraction of microcracks = 2%), whereas the NCA95 cathode particles cycled at the upper DOD of 60% were nearly fractured into individual primary particles with their areal fraction of microcracks at 16% even in the discharge state. Meanwhile, the NCA95 cathode cycled at the DOD of 100% contained a network of microcracks (areal fraction of microcracks = 8%) whose extent was considerably less than that of the same cathode cycled at the upper DOD of 60%. Hence, the microstructure of the cathode cycled at different DOD ranges is consistent with the cycling performance (Figure 1a). The impact of the DOD range on the microstructural stability of the NCA95 cathode was also confirmed by the R_{ct} measured during cycling at 67 mA g^{-1} (Figure 3d). The NCA95 cathode cycled at the three different DOD ranges exhibited a nearly similar R_{sf} (not shown herein), whereas the R_{ct} for the cathodes cycled at the upper DOD of 60% and DOD of 100% increased almost linearly with cycling such that the R_{ct} after 100 cycles reached 71.2 Ω for the upper DOD of 60% and 39 Ω for the DOD of 100%. Meanwhile, the R_{ct} for the NCA95 cycled at the lower DOD of 60% remained stable and was limited to 3.2 Ω. The above results clearly indicate that the NCA95 cathode cycled at the lower DOD of 60% is the most resistant to microcracking because the electrolyte penetration into the particle interior is reduced significantly during cycling.

Watanabe et al. extensively tested $Li[Ni_{0.76}Co_{0.14}Al_{0.10}]O_2$ at different DOD limits and widths and concluded that the capacity

DOI: 10.1021/acsenergylett.9b00733
ACS Energy Lett. 2019, 4, 1394−1400

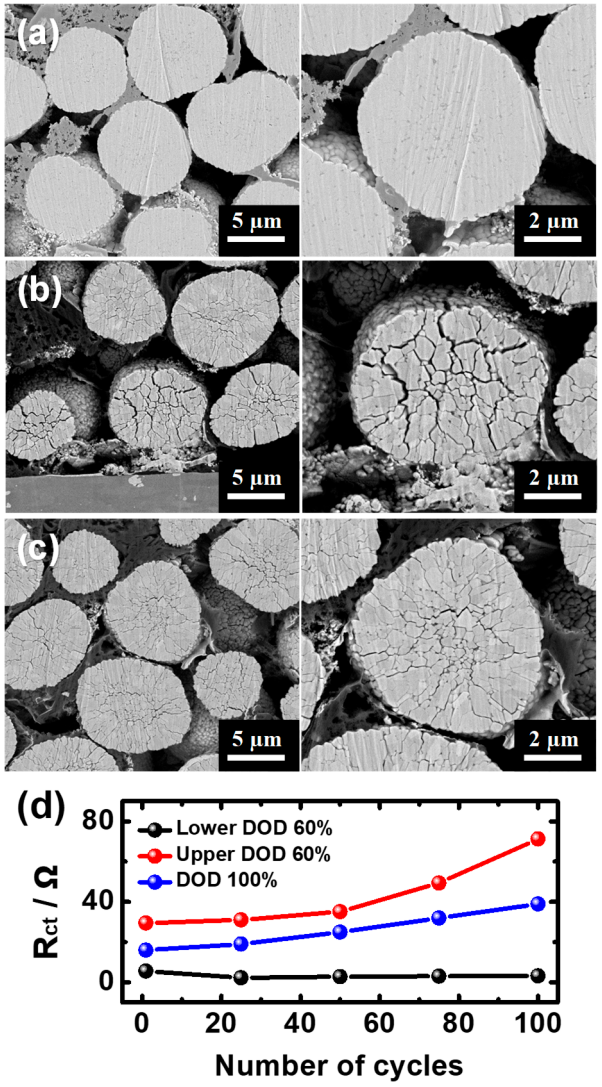

Figure 3. Cross-sectional SEM images of NCA95 cathodes after 100 cycles: (a) lower DOD of 60%, (b) upper DOD of 60%, and (c) DOD of 100%. (d) Variation in charge transfer resistance (R_{ct}) of NCA95 cathodes as a function of number of cycles.

retention of the cathode was not affected by the upper or lower DOD limits but was dictated by the DOD width.[21,22] It appears that their conclusion does not agree with the cycling performance dependence of the present NCA95 cathode on the DOD range. To further substantiate the DOD effect on the NCA cathode with different Ni fractions, the NCA80 and NCA88 cathodes were cycled at lower and upper DOD ranges at a current density of 67 mA g^{-1} (Figure S6 and Figure S7). As shown in Figure 4a,b, the NCA80 and NCA88 cathodes cycled at the lower DOD of 60% maintained their respective initial capacities with negligible losses (100% for NCA80 and 99.6% for NCA88). However, the Li intercalation stability decreased progressively with increasing Ni concentration when the two cathodes were cycled at the upper DOD of 60%. In comparison, the two cathodes cycled at the DOD of 100%, similar to the NCA95 cathode, tended to outperform the same cathodes at the upper DOD of 60% with the capacity retention of 95.7% vs 94.6% (upper DOD of 60%) for NCA 80 and 88.7% vs 86.8% (upper DOD of 60%) for NCA88. To further confirm the effect of upper DOD of 60% on microcracking, cross-sectional SEM images of the NCA80 and NCA88 cathodes charged to 4.3 V and discharged at upper DOD of 60% (3.73 V for NCA88 and 3.71 V for NCA80) were investigated (Figure 4c–f). The charged NCA80 cathode exhibited visible microcracks propagating from the particle core; however, the microcracks remained comparatively narrow and were arrested before reaching the particle outer surface. The areal fraction of the microcracks estimated from the cross-sectional image of the NCA80 cathode in Figure 4c was 9%. In the case of the charged NCA88 cathode in Figure 4e, the microcracks increased visibly in both density and width such that the areal fraction of the microcracks increased visibly in both density and width such that the areal fraction of the microcracks increased to 11%. More importantly, these microcracks propagated the particle surface, creating channels for electrolyte infiltration into the particle interior. Like NCA95 (Figure 2e, discharged to 3.76 V) but not so severe, the discharged NCA88 to 3.73 V also contained some visible residual microcracks (areal fraction of microcracks = 2%) that propagated to the particle surface. However, the discharged NCA80 to 3.71 V did not show any visible microcracks (areal fraction of microcracks = ~0%). As expected, the microcracks formed in the NCA80 cathode at 4.3 V almost completely closed back during discharge. From the above results, we believe that NCA cathodes with a Ni fraction below 0.8 are unlikely affected by the DOD limits; however, above 0.8, both the DOD width and limits increasingly dictate the cycling performance. Ni enrichment accelerates the microcrack formation proportionally; more importantly, the upper DOD limit determines the extent of microcracking during charge and the lower limit controls the microcrack closure during discharge.

To observe the extent of microcracking in the NCA80 cathode, cross-section SEM images of the cathode particles charged to 3.88 V (upper cutoff voltage of lower DOD of 60%) are shown in Figure S8. Compared to the SEM image of the NCA80 particles charged to 4.3 V (Figure 4c), the NCA80 particles charged to 3.88 V are relatively free of microcracks. To correlate the cycling performance with the extent of microcracking, the cross-sectional SEM images of the NCA80 cathode cycled at the three DOD ranges after 100 cycles are shown in Figure 5a–c. The NCA80 cycled at the lower DOD of 60% remained intact without any visible microcracks formation while the NCAs cycled at the upper DOD of 60% and DOD of 100% exhibit only hairline cracks that did not propagate to the particle surface. Although the former exhibits an increased amount of microcracks compared to the latter, which is in agreement with the cycling performance, the difference is small compared to the marked difference observed in the NCA95 cathode. The result reiterates that the DOD window becomes increasingly critical in stabilizing the cycle performance, especially when the Ni fraction in the NCA cathodes exceeds 0.8. This result also demonstrates that electrolyte penetration of the particle interior, even at the discharged state, must be minimized to mitigate the structural deterioration of the interior primary particles.

TEM analysis was also performed to verify the extent of structural damages incurred by the NCA95 cathode cycled at the upper 60% and full DOD ranges. A bright-field scanning TEM image of the NCA95 cathode cycled for 100 cycles in the upper DOD of 60% in Figure 6a shows a large crack that nearly fractures the secondary particle into two halves. In addition to the easily discernible intergranular microcrack, individual primary particles near the surface developed nanoscale intragranular cracks, as denoted by arrows in Figure 6b. A magnified image of the hairline crack near the primary particle surface in

DOI: 10.1021/acsenergylett.9b00733
ACS Energy Lett. 2019, 4, 1394–1400

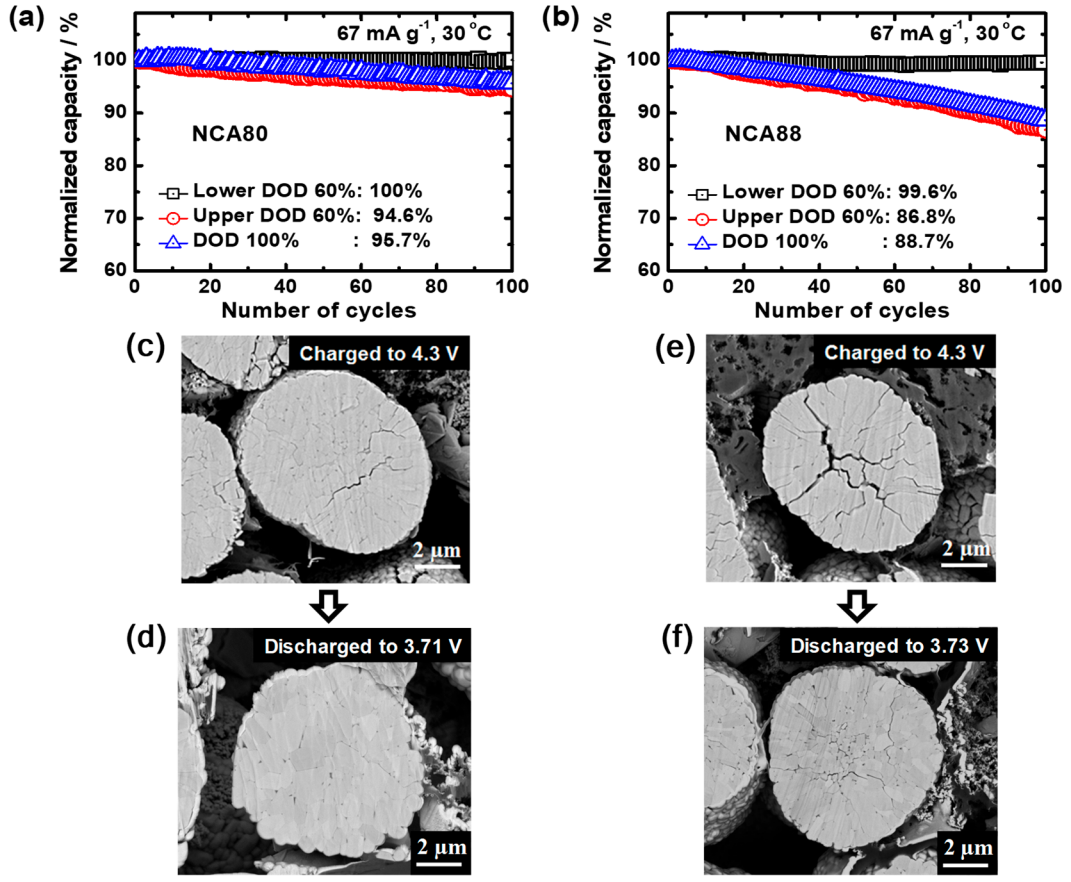

Figure 4. Cycle performances of (a) NCA80 and (b) NCA88 cathodes charged and discharged at different DOD ranges. Cross-sectional SEM images of NCA80 and NCA88 cathodes at first cycle: (c) charged NCA80 to 4.3 V, (d) charged NCA80 to 4.3 V and discharged to 3.71 V, (e) charged NCA88 to 4.3 V, and (f) charged NCA88 to 4.3 V and discharged to 3.73 V.

Figure 6c shows that the crack grew along the [001] direction through the layer planes, separating the primary particle into two halves by a gap of ∼5 nm. Numerous stacking faults or dislocations are also visible on the upper half produced by the anisotropic volume change. Further, ∼ 10 nm-thick alternating layers of the structural defects are observed in the interior of the primary particle. Upon magnification, we observed that the structural defects consisted of numerous dislocations and fine separation of the layer planes from the tensile strain generated during the detrimental H2−H3 transition. This accumulation of structural defects serves as an incipient stage of crack formation that will likely develop into a full crack upon cycling (Figure 6d−e). Examining the primary particle surface, a thin layer of 5−10 nm-thick NiO-like rocksalt (verified by the accompanying Fourier transform of the surface and bulk regions) that increases the impedance and hinders the Li migration is observed (Figure 6f). It appears that when the NCA95 cathode was discharged to 3.76 V, the stress state is not fully relieved and the buildup of the tensile strain not only initiates microcracks along the mechanically weak interparticle boundaries, but also undermines the mechanical integrity of the primary particle itself through the generation and accumulation of numerous structural defects. Moreover, the persistent microcracks in the discharged state, as shown in Figure 6e, expedite the electrolyte penetration and damage the interior primary particles severely, and will likely remain in the delithiated state during charging. An example of the severely damaged primary particle along a microcrack (marked as 'B" in Figure 6a) is shown in Figure 6g. SAED patterns of an area with a diameter of 100 nm are obtained along the primary particle. The initial layered structure diffraction pattern in the [100] zone transforms gradually to the [110] zone of the rocksalt structure as the alternating columns of diffraction spots disappeared gradually. The electrolyte attack along the microcrack is severe enough that the structural damage is not confined to the particle edges, as observed in the surface primary particles. Instead, the entire lower half of the primary particle in Figure 6g is converted to a rocksalt structure, attesting to the electrolyte penetration and subsequent structural damage that is assisted significantly by the incomplete closure of the microcracks in the discharged state. In comparison, the same NCA95 cathode cycled at DOD of 100% exhibited a similar structural damage as its bright-field scanning TEM image (in Figure 6h), and also contained a clearly visible crack that is arrested only near the secondary particle surface. A surface damage sustained by the surface particle is similar in that the thickness of the NiO-like rocksalt surface layer is also limited to ∼5 nm thick (Figure 6i,j). Figure 6j shows an intergranular microcrack formed in the observed primary particle; however, its width was confined to ∼1 nm, which is much narrower than that observed in the upper DOD of 60% cycled cathode. In the case of the NCA80 cathode cycled in the upper DOD of 60%, the structural damage is nearly nonexistent as the NCA80 cathode experiences a small amount of detrimental H2−H3 phase transition. A slight separation along the interparticle boundaries is observed in Figure 6k. A high-resolution TEM image of a surface primary particle from the upper DOD of 60%-cycled

DOI: 10.1021/acsenergylett.9b00733
ACS Energy Lett. 2019, 4, 1394−1400

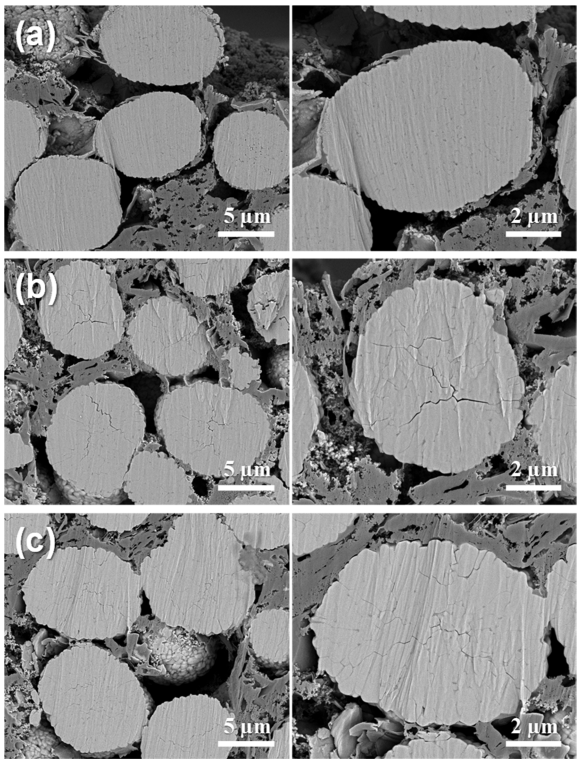

Figure 5. Cross-sectional SEM images of NCA80 cathodes after 100 cycles: (a) lower DOD of 60%, (b) upper DOD of 60%, and (c) DOD of 100%.

NCA80 cathode shows that the NiO-like rocksalt layer is nearly nonexistent (<1 nm) owing to the relatively low Ni fraction in the NCA80 cathode (Figure 6l,m). The post-mortem TEM analysis unequivocally confirms that cycling the NCA95 cathode in the upper DOD range strains the cathode particles severely, primarily because the anisotropic strain produced by the H2−H3 phase transition is not fully relieved and the persistent microcrack in the discharged state accelerates the structural deterioration of the interior primary particles. Finally, we plotted the capacity retention of the NCA80 and NCA95 cathodes cycled at the lower DOD of 60%, upper DOD of 60%, and DOD of 100% ranges against the areal fractions of the microcracks estimated from the cross-sectional images of the cycled cathodes (after 100 cycles) (Figure S9). An approximate linear relationship between capacity retention and microcracking extent well supports that the microcracking within the secondary particle is likely the primary source of the capacity fading observed in the Ni-rich NCA cathodes.

The electrochemical performance of Ni-enriched NCA80, NCA88, and NCA95 cathodes was intensively evaluated and correlated to the microcrack formation to determine the capacity fading mechanism of Ni-rich NCA cathodes. As observed in the NCM cathodes, increasing the Ni concentration in an NCA cathode led to higher reversible capacity: 202.5 mAh g^{-1} for NCA80, 219.8 mAh g^{-1} for NCA88, and 236.8 mAh g^{-1} for NCA95. However, the cycling performance of the cathodes deteriorated proportionally: capacity retention of 95.7% for NCA80, 88.7% for NCA88, and 85.5% for NCA95 after 100 cycles. It was found that the capacity retention of the Ni-enriched NCA cathodes was strongly dependent on the microcracking extent within the secondary particles. The microcracking was particularly detrimental to these cathodes because abundance of unstable Ni^{4+} species on the crack faces in contact with the infiltrated electrolyte caused rapid degradation of the internal exposed surfaces and buildup of impedance-increasing surface layer. Therefore, in the cases of highly Ni-enriched NCA cathodes, the DOD range and limits critically affected their cycling stabilities. In general, the upper portion of the DOD range was deleterious to the cycling stability because the anisotropic strain was not fully relieved and persistent microcracks in the discharged state facilitate electrolyte penetrated the particle interior. Consequent prolonged exposure

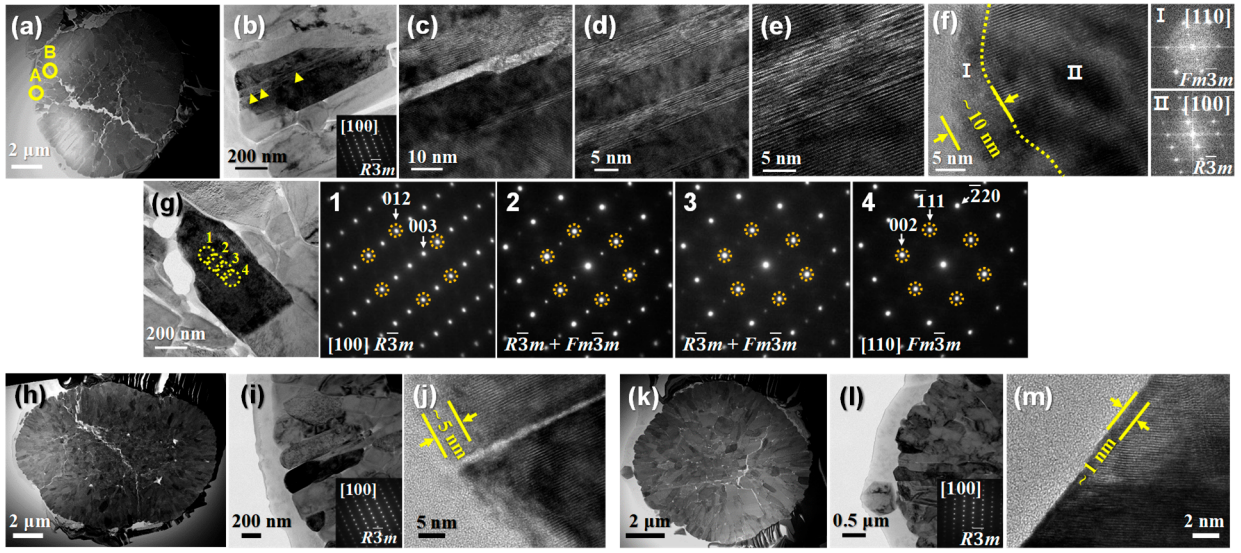

Figure 6. (a)−(g) TEM images of NCA95 cycled for 100 cycles in the upper DOD of 60%: (a) bright field STEM image, (b) magnified TEM image and SAED pattern (inset) from the region marked as "A" in (a), (c)−(e) high resolution TEM images from the regions marked in (b), (f) high-resolution TEM image of the primary particle surface with FFT pattern, and (g) magnified TEM image and SAED patterns from the region marked as "B" in (a). (h)−(j) TEM images of NCA95 cathode cycled for 100 cycles in the DOD of 100%: (h) bright field STEM image, (i) magnified TEM image, and (j) high-resolution TEM image. (k)−(m) TEM images of NCA80 cathode cycled for 100 cycles in the upper DOD of 60%: (k) bright field STEM image, (l) magnified TEM image, and (m) high-resolution TEM image.

DOI: 10.1021/acsenergylett.9b00733
ACS Energy Lett. 2019, 4, 1394−1400

of the interior primary particles to the electrolyte attack accelerated the structural damage and eventually undermined the mechanical integrity of the cathode particle.

■ ASSOCIATED CONTENT

Supporting Information

The Supporting Information is available free of charge on the ACS Publications website at DOI: 10.1021/acsenergylett.9b00733.

Experimental methods, XRD patterns, electrochemical charge−discharge curves, in-situ XRD patterns, cross-sectional SEM images, graph of areal fraction of microcracks vs capacity retention, structural parameters (PDF)

■ AUTHOR INFORMATION

Corresponding Authors

*E-mail: csyoon@hanyang.ac.kr (C.S.Y.).
*E-mail: yksun@hanyang.ac.kr (Y.-K.S.).

ORCID

Chong S. Yoon: 0000-0001-6164-3331
Yang-Kook Sun: 0000-0002-0117-0170

Notes

The authors declare no competing financial interest.

■ ACKNOWLEDGMENTS

This work was supported by a Human Resources Development Program (No. 20154010200840) of the Korea Institute of Energy Technology Evaluation and Planning (KETEP) grant funded by the Ministry of Trade, Industry and Energy of the Korean government, and by the Global Frontier R&D Programme (2013M3A6B1078875) on the Center for Hybrid Interface Materials (HIM), by the Ministry of Science and ICT.

■ REFERENCES

(1) *DoE Annual Merit Review* 2018, http://www.annualmeritreview.energy.gov/.
(2) Dahn, J. R.; Sacken, U. V.; Michal, C. A. Structure and electrochemistry of $Li_{1\pm y}NiO_2$ and a new Li_2NiO_2 phase with the $Ni(OH)_2$ structure. *Solid State Ionics* **1990**, *44*, 87−97.
(3) Delmas, C.; Saadoune, I.; Rougier, A. The cycling properties of the $Li_xNi_{1-y}Co_yO_2$ electrode. *J. Power Sources* **1993**, *44*, 595−602.
(4) Liu, Z.; Yu, A.; Lee, J. Synthesis and characterization of $LiNi_{1-x-y}Co_xMn_yO_2$ as the cathode materials of secondary lithium batteries. *J. Power Sources* **1999**, *81*−*82*, 416−419.
(5) Ohzuku, T.; Makimura, Y. Layered Lithium Insertion Material of $LiCo_{1/3}Ni_{1/3}Mn_{1/3}O_2$ for Lithium-Ion Batteries. *Chem. Lett.* **2001**, *30*, 642−643.
(6) Shim, J.; Kostecki, R.; Richardson, T.; Song, X.; Striebel, K. A. Electrochemical analysis for cycle performance and capacity fading of a lithium-ion battery cycled at elevated temperature. *J. Power Sources* **2002**, *112*, 222−230.
(7) Guilmard, M.; Pouillerie, C.; Croguennec, L.; Delmas, C. Structural and electrochemical properties of $LiNi_{0.70}Co_{0.15}Al_{0.15}O_2$. *Solid State Ionics* **2003**, *160*, 39−50.
(8) Yoon, C. S.; Jun, D.-W.; Myung, S.-T.; Sun, Y.-K. Structural Stability of $LiNiO_2$ Cycled above 4.2 V. *ACS Energy Lett.* **2017**, *2*, 1150−1155.
(9) Lim, B.-B.; Myung, S.-T.; Yoon, C. S.; Sun, Y.-K. Comparative Study of Ni-Rich Layered Cathodes for Rechargeable Lithium Batteries: $Li[Ni_{0.85}Co_{0.11}Al_{0.04}]O_2$ and $Li[Ni_{0.84}Co_{0.06}Mn_{0.09}Al_{0.01}]O_2$ with Two-Step Full Concentration Gradients. *ACS Energy Lett.* **2016**, *1*, 283−289.
(10) Sun, Y.-K.; Myung, S.-T.; Park, B.-C.; Parakash, J.; Belharouak, I.; Amine, K. High-energy cathode material for long-life and safe lithium batteries. *Nat. Mater.* **2009**, *8*, 320−324.
(11) Noh, H.-J.; Youn, S.; Yoon, C. S.; Sun, Y.-K. Comparison of the structural and electrochemical properties of layered $Li[Ni_xCo_yMn_z]O_2$ (x = 1/3, 0.5, 0.6, 0.7, 0.8 and 0.85) cathode material for lithium-ion batteries. *J. Power Sources* **2013**, *233*, 121−130.
(12) Sun, H.-H.; Choi, W.; Lee, J.; Oh, I.-H.; Jung, H.-G. Control of electrochemical properties of nickel-rich layered cathode materials for lithium ion batteries by variation of the manganese to cobalt ratio. *J. Power Sources* **2015**, *275*, 877−883.
(13) Yoon, C. S.; Choi, M. H.; Lim, B.-B.; Lee, E.-J.; Sun, Y.-K. Review—High-Capacity $Li[Ni_{1-x}Co_{x/2}Mn_{x/2}]O_2$ (x = 0.1, 0.05, 0) Cathodes for Next-Generation Li-Ion Battery. *J. Electrochem. Soc.* **2015**, *162*, A2483−A2489.
(14) Kim, U.-H.; Jun, D.-W.; Park, K.-J.; Zhang, Q.; Kaghazchi, P.; Aurbach, D.; Major, D. T.; Goobes, G.; Dixit, M.; Leifer, N.; Wang, C. M.; Yan, P.; Ahn, D.; Kim, K.-H.; Yoon, C. S.; Sun, Y.-K. Pushing the limit of layered transition metal oxide cathodes for high-energy density rechargeable Li ion batteries. *Energy Environ. Sci.* **2018**, *11*, 1271−1279.
(15) Zhou, P.; Meng, H.; Zhang, Z.; Chen, C.; Lu, Y.; Cao, J.; Cheng, F.; Chen, J. Stable layered Ni-rich $LiNi_{0.9}Co_{0.07}Al_{0.03}O_2$ microspheres assembled with nanoparticles as high-performance cathode materials for lithium-ion batteries. *J. Mater. Chem. A* **2017**, *5*, 2724−2731.
(16) Ryu, H.-H.; Park, K.-J.; Yoon, C. S.; Sun, Y.-K. Capacity Fading of Ni-Rich $Li[Ni_xCo_yMn_{1-x-y}]O_2$ ($0.6 \le x \le 0.95$) Cathodes for High-Energy-Density Lithium-Ion Batteries: Bulk or Surface Degradation? *Chem. Mater.* **2018**, *30*, 1155−1163.
(17) Yoon, C. S.; Ryu, H.-H.; Park, G.-T.; Kim, J.-H.; Kim, K.-H.; Sun, Y.-K. Extracting maximum capacity from Ni-rich $Li[Ni_{0.95}Co_{0.025}Mn_{0.025}]O_2$ cathodes for high-energy-density lithium-ion batteries. *J. Mater. Chem. A* **2018**, *6*, 4126−4132.
(18) Yoon, C. S.; Jun, D.-W.; Myung, S.-T.; Sun, Y.-K. Structural Stability of $LiNiO_2$ Cycled above 4.2 V. *ACS Energy Lett.* **2017**, *2*, 1150−1155.
(19) Kondrakov, A. O.; Schmidt, A.; Xu, J.; Geßwein, H.; Mönig, R.; Hartmann, P.; Sommer, H.; Brezesinski, T.; Janek, J. Anisotropic Lattice Strain and Mechanical Degradation of High- and Low-Nickel NCM Cathode Materials for Li-Ion Batteries. *J. Phys. Chem. C* **2017**, *121*, 3286−3294.
(20) Lim, J.-M.; Hwang, T.; Kim, D.; Park, M.-S.; Cho, K.; Cho, M. Intrinsic Origins of Crack Generation in Ni-rich $LiNi_{0.8}Co_{0.1}Mn_{0.1}O_2$ Layered Oxide Cathode Material. *Sci. Rep.* **2017**, *7*, 39669.
(21) Watanabe, S.; Kinoshita, M.; Hosokawa, T.; Morigaki, K.; Nakura, K. Capacity fading of $LiAl_yNi_{1-x-y}Co_xO_2$ cathode for lithium-ion batteries during accelerated calendar and cycle life tests (effect of depth of discharge in charge−discharge cycling on the suppression of the micro-crack generation of $LiAl_yNi_{1-x-y}Co_xO_2$ particle). *J. Power Sources* **2014**, *260*, 50−56.
(22) Watanabe, S.; Kinoshita, M.; Hosokawa, T.; Morigaki, K.; Nakura, K. Capacity fade of $LiAl_yNi_{1-x-y}Co_xO_2$ cathode for lithium-ion batteries during accelerated calendar and cycle life tests (surface analysis of $LiAl_yNi_{1-x-y}Co_xO_2$ cathode after cycle tests in restricted depth of discharge ranges). *J. Power Sources* **2014**, *258*, 210−217.
(23) https://www.tesla.com, accessed May 2019.

DOI: 10.1021/acsenergylett.9b00733
ACS Energy Lett. 2019, 4, 1394−1400